

Observation of coherent Drift-Rotational modes with Strong Driven Rotation on the Large Plasma Device

D.A. Schaffner,¹ T.A Carter,¹ G.D. Rossi,¹ D.S. Guice,¹ J.E. Maggs,¹ S. Vincena,¹ and B. Friedman¹

Department of Physics and Astronomy, University of California, Los Angeles

(Dated: 24 October 2013)

The instabilities observed on the Large Plasma Device (LAPD) [W. Gekelman, *et. al*, Rev. Sci. Instr. **62**, 2875 (1991)] are explored in conjunction with the ability to finely adjust azimuthal flow and flow shear.

I. INTRODUCTION

The nature of the types of instabilities found in the LAPD plasmas can have important effects on the resulting turbulence and transport. One example of this effect is in the scaling of turbulence and transport suppression with shear as discussed in the variations of decorrelation models of shear suppression which make different assumptions on the instabilities present and driving the turbulence⁷. Instability identification in a turbulent setting can be an extremely difficult task as there are many simultaneous sources of free energy as well as the fact that non-linear fluctuation behavior can be vastly different than the linear modes that might originate it. Nevertheless, mode identification (or at least categorization) can be useful in understanding the physical mechanisms in turbulence and transport so any attempt is worthy.

This biasing experiment in LAPD provides a useful approach to mode identification as it has been shown that biasing can significantly modify the plasma gradients present thus changing the drive of different linear instabilities. The three main linear instabilities that will be analyzed in this section are the resistive drift-wave (hereafter DW), the rotational interchange mode (RI), and the Kelvin-Helmholtz instability (KH). The resistive pressure-gradient driven instability or drift-wave has been shown to be present in the LAPD in⁷. Investigations and identification of the KH mode was made on the LAPD in⁷. Linear calculations using a Braginskii fluid model (discussed later in the section) has shown that given experimental profiles—those taken from previous biasing experiments on LAPD^{6,7}—the activity of all three of these instabilities are present and the growth rates for all three modes are comparable⁷.

Simulations of LAPD turbulence using the BOUT++ code have revealed the presence of a nonlinear instability which overtakes the linear modes in establishing the resulting turbulent state³². Thus it is possible that linear modes do not have any connection to the turbulent state in LAPD. It should be noted however, that simulations have only been performed for the "null flow" state and that linear instabilities may explain the fluctuation spectrum (in particular the coherent mode) at higher biases.

Since the experimental data is taken from the steady-state portion of the plasma discharge, when growing linear instabilities will not only have already saturated, but will likely have already non-linearly interacted to form a broadband turbulent state, mode identification cannot

rely entirely on the clues from the fluctuation and spectral data. The spectral information is combined with examination of location and strength of gradients which can drive the instabilities, the direction of propagation of these modes and comparison to the growth rates and frequencies of linear modes as calculated using a Braginskii fluid equation eigenfunction solver to narrow down the likelihood of contributions to the turbulence due to each of the three instabilities. The appearance of a distinct coherent mode in the highest biases is also helpful in distinguishing between mode types especially when compared to linear growth rates. While a full 3D non-linear simulation like BOUT++ can provide much better comparisons, the combination of the approaches mentioned can be highly suggestive.

The varying features of the spectral density functions—calculated using the two-point correlation technique—are used to distinguish amongst modes. By calculating the spectral density for different regions and different groupings of bias states, the features can be used to compare to both radial and bias locations of driving gradients as well as to growth rates from linear calculations restricted to similar spatial regions and bias groupings.

II. WAVENUMBER-FREQUENCY SPECTRAL DENSITY

In addition to temporal fluctuation spectra, spatial spectra can be used to analyze turbulent properties of the plasma. The most accurate way to determine a spatial spectrum—that is, the distribution of fluctuation power broken into spatial eigenmodes—would be to have a simultaneous measurement of plasma parameters (I_{sat}, V_f) at a high resolution of multiple positions. While this can be partly achieved using multiple tipped Langmuir probes (such as the rake probe described in Chapter 3), such a probe offers far too little spatial resolution to be of very much use. Instead, the high temporal resolution available to the Langmuir probe signals can be used to approximate a local wavenumber spectrum using a two-point correlation technique. This method uses the time correlation between two points to measure a relative phase, and with a known separation distance, a local wavenumber, $k_l = \theta/d$. Given a large enough number of statistics, a distribution of local wavenumber as a function of frequency and position can be created. The details of this process are discussed in detail in Appendix

B. The results of such an analysis yield spectral density functions which is a histogram of fluctuation power binned by wavenumber and frequency.

Since the LAPD is a cylindrical device, it is most natural to cast eigenmodes of the system with as having an azimuthal component $\sim e^{im\theta}$ with mode number, m; an axial component $\sim e^{inz}$, with eigenvalue n; and a radial eigenfunction $f(r)$. The stability of the relevant modes depend most on the azimuthal mode number, m, (and consequently the resulting transport) and is thus of most interest for turbulence study. Though m-numbers are the more physically relevant quantity, the two-point correlation method used here determines an azimuthal wavenumber first, where $k_\theta = m/r$. The results will be shown first cast in terms of k_θ and a frequently used ratio, $k_\theta \rho_s$, but will also be shown in terms of azimuthal mode numbers.

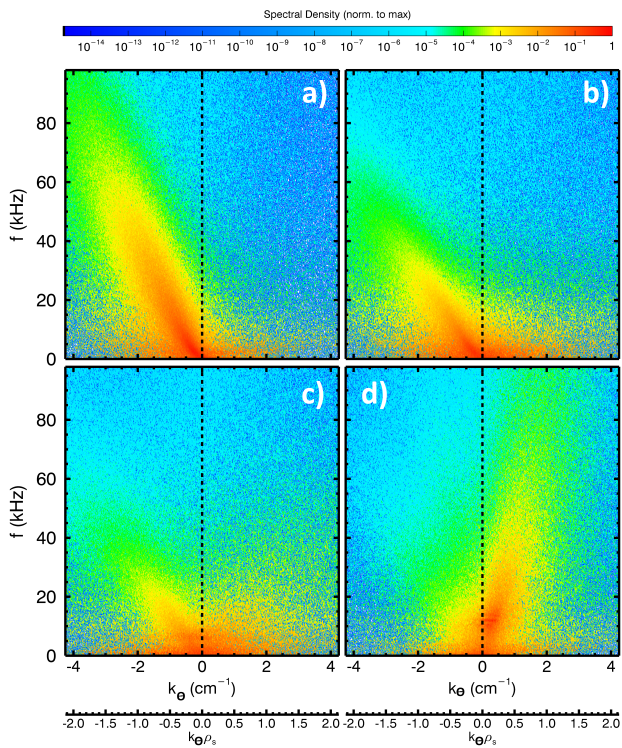


FIG. 1. Perp Wavenumber spectra for four different bias groups (a)Low/Unbiased IDD flow Bias0-2, (b)Min Flow Bias10-12 (c)Low EDD Flow Bias 16-18 and (d)Strong EDD flow Bias 25-27.

The global changes in power frequency and wavenumber space as a function of bias can be seen in Figure 1. The spectral amplitude is histograms into bins 312Hz wide in frequency, and 0.01 cm^{-1} wide in wavenumber space. Spectral density histogram (a) is averaged over all radial locations from 12-32cm and over Bias 0,1, and 2, which are essentially all unbiased cases (they are all biases less than the floating potential). Histogram (b) shows the average of three biases around where the plasma rotation nulls out—Bias 10,11 and 12. Histogram

(c) averages biases in the low to medium EDD flow regime—Bias 16,17, and 18. Finally, Histogram (d) averages some strong EDD flow biases—Bias 25,26 and 27.

As with the line plots above, these spectral density functions show the overall shift in propagation direction for the modes as the bias is increased. These plots show that the vast majority of the fluctuation power resides in the frequency space less than 10kHz and within a wavenumber space less than 2.0 cm^{-1} or, assuming an ion sound radius of $\rho_s \sim 0.5\text{cm}$, within a $k_\perp \rho_s < 1$. Power does expand out into a narrow band that increases approximately linearly in both frequency and wavenumber. In the unbiased state, a line fit along this strip would have a slope that corresponded to a phase velocity, $v_p = f/k = 2 \times 10^4 \text{ cm/s}$ which is about an order of magnitude less than the peak flows observed in this state. This confirms that these distributions are not set entirely by the Doppler shift.

As the bias is increased to the point where plasma rotation minimized, fluctuation amplitude begins to be concentrated toward smaller wavenumber and frequency. Both the frequency and wavenumber of the linear feature in the IDD direction decreases and its slope decreases slightly to a phase velocity of $1.5 \times 10^4 \text{ cm/s}$ which shows the slight impact of Doppler shifting on phase velocity. There is also slightly more power in the EDD direction. It should be noted, though that even in the minimum flow state, there is still moderate amounts of flow in the IDD at the far edge or $r > 30\text{cm}$ as can be seen in Figure ???. In fact, the far edge flow appears to be consistently in the IDD beyond 30cm even for the flow states with the highest peak driven flow. This can be seen in these four plots by the presence of power in the IDD which is never completely eliminated.

For biases that cause plasma to rotate at low to medium rates in the EDD direction, as in Figure ??(c), there is a clear difference in distribution for modes that propagate in the EDD and those still propagating in the IDD. The IDD modes maintain the narrow lobe shape that is reminiscent of the unbiased case and can somewhat still be fit by a linear dispersion relation with phase velocity on the order of $\sim 1.5 - 2 \times 10^4 \text{ cm/s}$. The EDD modes on the other hand are more broadly distributed in the range from 0-40kHz and $0-4 \text{ cm}^{-1}$. No dispersion relation can be approximated in this region. This difference is perhaps an indication of differing origins of the turbulence and evidence that the biasing is changing the free energy drive of the turbulent fluctuations.

The highest measured biases show the most significant change in the spectral distribution showing both the coherent mode at approximately $f=10\text{kHz}$ and $k=0.5\text{cm}^{-1}$, but also fluctuation power in modes propagating predominantly in the EDD direction. Rather than being diffuse, a narrow lobe is formed like in the unbiased state, but with a steeper slope. An approximate fit to this slope yields a phase velocity more like $v_p \sim 4 \times 10^4 \text{ cm/s}$. This could be due to a change in the underlying instability drive and resulting mode, or from the influence of the

stronger EDD rotation in this state. Nevertheless, there is a clear transition in the nature of the turbulence not only from the unbiased state to the high biased, high rotation state, but even between the lower EDD rotation and higher EDD rotation states as in Figure ??(c) and (d).

III. OBSERVATION OF COHERENT MODES

Fluctuation data from a recently conducted study of finely controlled azimuthal rotation on the LAPD⁸ shows the emergence of a coherent mode with increasing limiter bias and thus azimuthal flow.

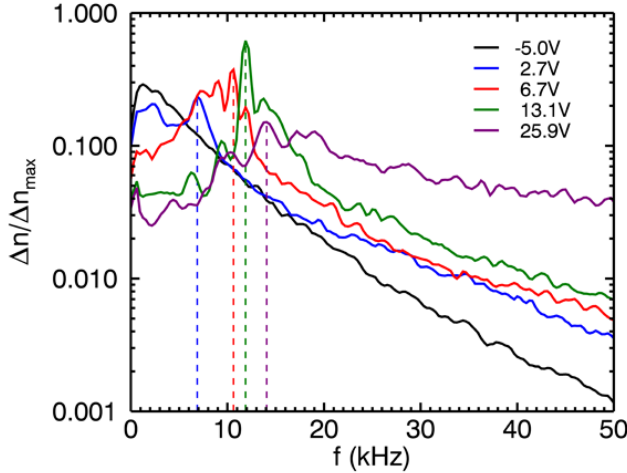


FIG. 2. Coherent modes for various biases

Figure 2 shows the frequency spectra for various biases for frequencies up to 50kHz and focused in the region right around the limiter edge, where the presence of the coherent mode is strongest. Compared to the minimum flow case (Limiter-Anode = -5.0V), where the fluctuation spectrum is broadband, a clear peaks in the spectra emerge starting at a Limiter-Anode voltage difference of 2.7V and increasing in power and frequency up to a voltage difference of 13.1V. The highest bias listed, with a voltage difference of 25.9V, shows a reduction in power and less distinct peaks.

The mode is shown to be highly localized at the limiter edge.

Figure 3 shows the spatial distribution of turbulent fluctuations for four different biases: (a) an unbiased state with small IED flow, (b) a minimum shearing state, (c)a small EDD flow, and (d) a strong EDD flow state. Each of the four contour plots show the logarithm of the density fluctuation power as a function of both radius and frequency with the limiter edge indicated by the dashed line at 26cm. All four plots are normalized to the same maximum fluctuation value. In the first plot, (a), the fluctuation power is generally fairly evenly distributed radially. As mentioned before, most of the fluctuation

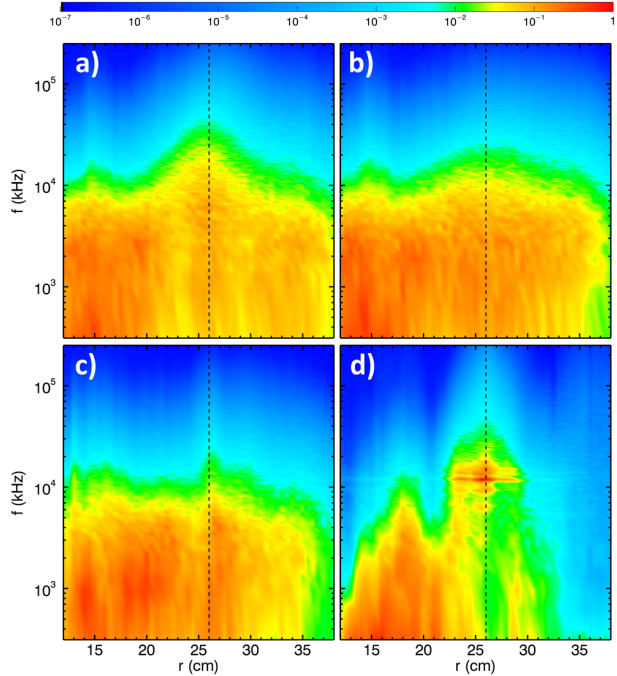


FIG. 3. Contour Plots of Density fluctuation power (normalized to the maximum value) versus frequency and radius for (a)0bias, (b)Bias 7, (c)Bias18, (d)Bias27

power is concentrated in the band < 10kHz. There is a slight spreading of power in frequency at the limiter edge. This could be due partially to Doppler shifting of the frequency from the spontaneous flow, though the peak flow in this stage occurs at about 28cm. There is also a local maximum of fluctuation amplitude at the limiter edge.

Though the previous spectral distribution plots showed that the core region usually had a smaller amount of fluctuation power overall, in this very low frequency regime, the core region tends to have the highest absolute fluctuation amplitude. Evidence for this trend was also observed in the fluctuation profiles as in Figure ???. However, as that same figure shows, it is clear that the core region generally has the lowest percentage fluctuation amplitude when compared to the density level.

Figures 3(b) and 3(c) show the modification of the spatial distribution as the limiter bias is increased to -6.3V below the anode(b) and 0.22V above the anode(c) respectively. The -6.3V bias has low flow and nearly zero shear. The fluctuation power is shifted back toward lower frequencies as seen in the line cut plots and is even more evenly spatially distributed than the unbiased state.

As the bias surpasses the anode voltage in (c) and the flow begins to go in the opposite azimuthal direction, the main effect appears to be a decrease in fluctuation amplitude in the edge region. One of the coherent modes can be seen emerging at the limiter edge at about 5kHz. Finally in Figure 3(d), at a bias of 13.1V above the anode and in a highly EDD flowing state, the highest fluctuation power appears in the coherent mode now at a fre-

frequency of 10kHz. Fluctuations outside the limiter edge are almost completely removed, having decreased an order of magnitude or more compared to their peak values. Even the core fluctuations are spatially modified with peaks concentrated in the region between 15 and 20cm. This core change could be related to a modification of the density gradient which actually slightly reverses to point outward in this 15–20cm region as can be seen in Figure ???. Clearly, though, the most change in spatial turbulence occurs in the higher biases, with the highest rotation states achieved. Since the free-energy sources are most modified by the biases—steepest density gradients, highest flow and flow shear states—it's very likely the turbulence modification is due to this change in drive.

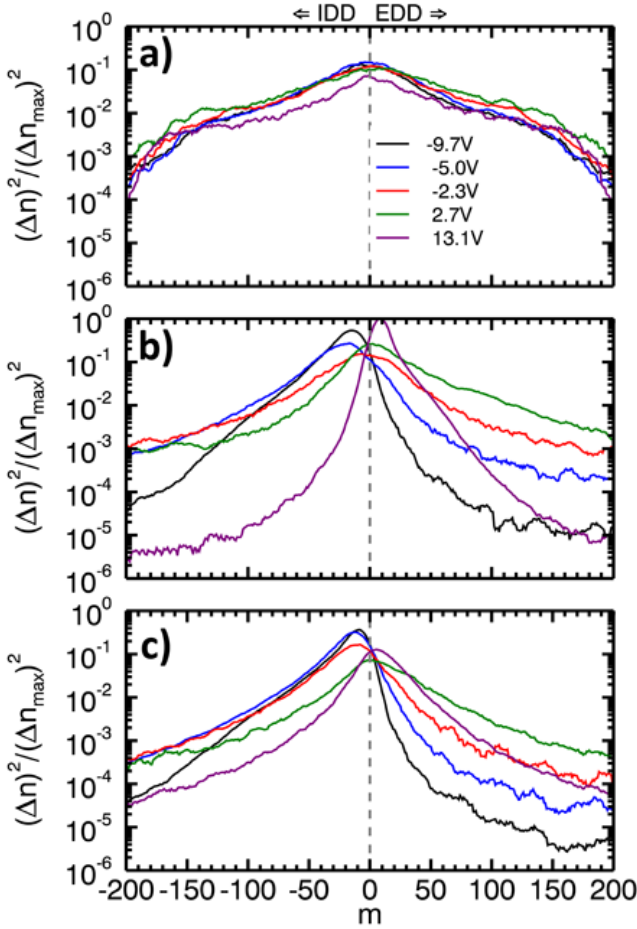


FIG. 4. Azimuthal mode number m spectra for (a) core, (b) transition, and (c) edge regions for various bias states

Returning to the wavenumber/M-number spectra, a plot of the total power for each M-number is shown in Figure 4. From this plot, it can be seen that the peak mode number in the unbiased edge regions is about $m=15$. At the limiter edge, this corresponds to a wavenumber of $k = m/r = 0.577\text{cm}^{-1}$ or a wavelength of $\lambda = 10.9\text{cm}$. In the strongly biased regime, the peak switches to $m=10$ in the EDD direction which is $k = 0.384$ or $\lambda = 16.3\text{cm}$ at the limiter edge. Since the

growth of the coherent mode is strongest at the limiter edge, its is likely that these modes generate the peak at $m=10$.

IV. COMPARISON TO A LINEAR FLUID MODEL

To elucidate the contribution among mode types in the LAPD turbulence, it is useful to compare to results to a Braginskii fluid model which attempts to closely represent the collisional LAPD plasma. The following section discusses comparison between linear growth rates as calculated from a linearized set of Braginskii fluid equations with the fluctuation amplitudes as measured experimentally. While there is obvious interpretive difficulty in attempting to match saturated turbulent fluctuation amplitude with calculated growth rates of linear modes, any connects observed can be used to in concert with many experimental observations to get an idea of what physical processes may be at work.

The basic Braginskii fluid equations combine the density, ion momentum and electron momentum and charge conservation equation with collisional damping amongst ions, electrons and neutrals included:

$$\frac{\partial}{\partial t}(N) + (\mathbf{v}_e \cdot \nabla)N = 0 \quad (1)$$

$$Nm_e \left(\frac{\partial}{\partial t}(\mathbf{v}_e) + (\mathbf{v}_e \cdot \nabla)\mathbf{v}_e \right) = -\nabla(Nk_bT_e) - Ne \left(\mathbf{E} + \frac{\mathbf{v}_e}{c} \times \mathbf{B} \right) - Nm_i \nu_{in} \mathbf{v}_i \quad (2)$$

$$Nm_i \left(\frac{\partial}{\partial t}(\mathbf{v}_i) + (\mathbf{v}_i \cdot \nabla)\mathbf{v}_i \right) = -Ne \left(\mathbf{E} + \frac{\mathbf{v}_i}{c} \times \mathbf{B} \right) - Nm_i \nu_{in} \mathbf{v}_e \quad (3)$$

$$\nabla \cdot (eN(\mathbf{v}_{i\parallel} - \mathbf{v}_{e\parallel}) + eN(\mathbf{v}_{i\perp} - \mathbf{v}_{e\perp})) = 0 \quad (4)$$

The following equations are a modified set of Braginskii fluid equations—augmented by the inclusion of radial density diffusion and ion-ion viscosity—used in an eigenmode solver code to calculate the growth rates and associated radially eigenfunctions of the modes present.

$$\frac{\partial}{\partial t}(N) = -\mathbf{v}_E \cdot \nabla N - \frac{\partial}{\partial z}(v_{\parallel e}N) - D_n \nabla_{\perp}^2 N \quad (5)$$

$$\frac{\partial}{\partial t}(v_{\parallel e}) = -\mathbf{v}_E \cdot \nabla v_{\parallel e} - \frac{m_i}{m_e} \frac{T_{e0}}{N_0} \frac{\partial}{\partial z}(N) - \frac{m_i}{m_e} \frac{\partial}{\partial z}(\phi) + 1.71 \frac{m_i}{m_e} \frac{\partial}{\partial z}(T_e) \quad (6)$$

$$\frac{\partial}{\partial t}(\varpi) = -\mathbf{v}_E \cdot \nabla \varpi - \frac{\partial}{\partial z}(v_{\parallel e}N) + b \times \nabla N \cdot \frac{\nabla^2 v_E}{2} - \nu_{in} \varpi - \mu_{ii} \nabla_{\perp}^2 \varpi \quad (7)$$

where $\varpi = \nabla_{\perp} \cdot (N \nabla_{\perp} \phi)$ is the definition of vorticity. Cast in cylindrical geometry, with $\mathbf{x} = (r, \theta, z)$, the solutions of the form

$$f(\mathbf{x}) = f(r) \exp(im_{\theta}\theta + ik_{\parallel}z - i\omega t) \quad (8)$$

are sought for density, N , parallel electron flow, $v_{\parallel e}$, and vorticity, ϖ , where m_θ is the azimuthal mode number and k_\parallel is the axial wavelength which can be case in terms of an axial eigenvalue, n_z .

The origins of the three different instabilities can be highlighted from the many various terms in Equations 7. First the growth of resistive drift-waves can be narrowed down to the following subset of equations,

$$\frac{\partial}{\partial t}(N) = -\mathbf{v}_E \cdot \nabla N - \frac{\partial}{\partial z}(v_{\parallel e}N) \quad (9)$$

$$\frac{\partial}{\partial t}(v_{\parallel e}) = -\mathbf{v}_E \cdot \nabla v_{\parallel e} - \frac{m_i}{m_e} \frac{T_{e0}}{N_0} \frac{\partial}{\partial z}(N) - \frac{m_i}{m_e} \frac{\partial}{\partial z}(\phi) - \nu_e v_{\parallel e} \quad (10)$$

$$\frac{\partial}{\partial t}(\varpi) = -\frac{\partial}{\partial z}(v_{\parallel e}N) \quad (11)$$

which highlight the DW drive dependence on the gradient in density as well as the parallel electron response. In order for the DW to be unstable, a phase shift between the density and plasma potential is necessary and in these equations is provided by the resistivity due to electron collisions (found in the term $\nu_e v_{\parallel e}$).

Similarly, the origin of rotational interchange is contained in the subset,

$$\frac{\partial}{\partial t}(N) = -\mathbf{v}_E \cdot \nabla N \quad (12)$$

$$\frac{\partial}{\partial t}(\varpi) = -\mathbf{v}_E \cdot \nabla \varpi + b \times \nabla N \cdot \frac{\nabla^2 v_E}{2} - \nu_{in} \varpi \quad (13)$$

where the $b \times \nabla N \cdot \frac{\nabla^2 v_E}{2}$ terms serves as the centrifugal force terms which initiates the mixing inherent in the interchange instability.

Lastly, the KH modes arise due to the gradient in the vorticity as in,

$$\frac{\partial}{\partial t}(\varpi) = -\mathbf{v}_E \cdot \nabla \varpi \quad (14)$$

The remaining terms represent dissipative effects including perpendicular diffusion contained in the term $D_n \nabla_\perp^2 N$, where D_n taken to be classical diffusion in the code, and damping due to ion-ion viscosity contained in the term $\mu_{ii} \nabla_\perp^2 \varpi$.

Of course, in the full set of equations coupling can take place between modes (e.g. drift-interchange modes). However, it should be noted that drift waves can only occur when a parallel wavelength is present; in other words, when there is a non-zero parallel eigennumber, n . For $n=0$, only rotational interchange and Kelvin-Helmholtz modes can be active. For comparisons to these experiments, only values of $n_z = 0$ and 0.5 are used which correspond to infinite wavelength flute-like modes for $n_z = 0$ and wavelengths of the order of twice the machine length ($n_z = 0.5$), similar to the fundamental mode of a column with one open boundary condition and one closed boundary condition.

Using experimental profiles of density, temperature, and plasma potential for a given bias, Equations 7 are

solved as an algebraic eigenvalue problem for each azimuthal eigenmode number, m , and parallel eigenmode number, n . The range of m numbers used for this analysis was $m = 1 - 80$ while $n=0$ or 0.5 as mentioned previously. The solutions consist of radial eigenfunctions for density, parallel velocity, and plasma potential of the form in Equation 8 coupled with a growth rate, γ , and a frequency, $\omega = 2\pi f$. A positive(negative) growth rate indicates an unstable(stable) mode while the sign of the frequency indicates the propagation direction of the mode. For this analysis, only the density eigenfunctions, growth rates and frequencies were used.

Figure 5 shows typical results from the profiles of four different biases(Bias#/(Limiter-Anode) potential : (a) Bias 1/-9.7V representing the unbiased IDD flow state, (b) Bias 8/-4.1V representing the zero flow state, (c) Bias 20/3.7V represented the moderate EDD flow state and (d) Bias 27/13.1V representing the strong EDD flow state. The growth rate and mode number for the fastest growing mode for each m -number is shown with the blue curves indicating calculations for $n=0$ and green for $n=0.5$. The mode selected is restricted to have a peak in its corresponding density eigenfunction within the a certain radial range; here, the modes are selected to be within radii of 20 and 32cm. If the fastest growing mode does not have a peak in its eigenfunction within the selected range, the next fastest growing mode is chosen and so on until all the possible modes are exhausted. This procedure ensures comparison to modes driven by the experimentally relevant gradients and not due to numerical artifacts.

The variations amongst the four biases shown demonstrate how the linear growth of instabilities are modified by the changes in the plasma profiles. In general, the $n=0$ modes appear to dominate the growth when both are present, certainly at lower m numbers. The exceptions are for small regions in the unbiased case and for m numbers larger than 20 in the moderate EDD flow case. In the zero flow case, only drift-waves can be active so only $n=0.5$ modes will be unstable. The portions of Figure 5 which show the frequency of the corresponding growing mode indicate the direction of propagation of the modes. In the unbiased case, the $n=0$ modes propagate in the positive direction which given the experimental arrangement corresponds to the IDD direction. In the EDD flow biases, the frequency sign is now negative indicating propagation in the EDD direction. In the highest bias shown, the frequencies are in the EDD for all m numbers suggesting that all of these modes are predominately interchange driven modes. The moderate EDD mode has frequencies in both directions. The lower m number modes are likely rotational interchange, but the higher m number modes can either be interchange modes driven by flow in the IDD (which does occur in the very far radial end of this bias) or are KH modes which do not have to propagate in the direction of the flow. The zero flow state with only drift waves shows that drift-waves propagate only in the EDD.

In order to facilitate comparisons to the experimen-

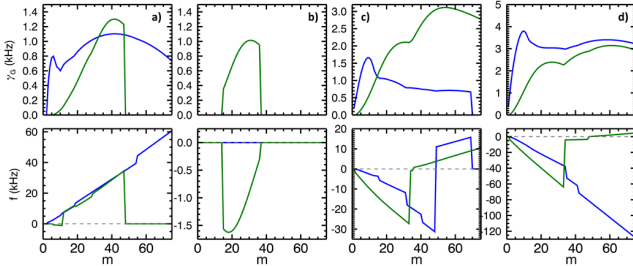


FIG. 5. Plots of the linear calculated growth rate and frequency of the fastest growing mode for each m number. Blue curves represent calculations using $n=0$. Green curves represent calculations with $n=0.5$. Column(a) shows calculations for Bias 1, (b) for Bias 8, (c) for Bias 20 and (d)for Bias 27.

tal spectral density functions, a “growth rate density” function is constructed using the eigenfunctions, growth rates and frequencies of the Braginskii equation solutions. First, the normalized eigenfunction of the fastest growing mode for each m number is scaled to the value of the growth rate to create a localized growth function—that is, the strength of the growing mode is maximum at the peak of the eigenfunction and reduced accordingly away from the peak. This radial distribution of growth rate is broken into wavenumbers, k , given the m number and radius. Connected to each value of k is the frequency of the mode, and the sign of the frequency is converted into a sign of the wavenumber. Then, this collection of signed wavenumbers or frequencies is histogrammed into wavenumber and frequency bins and then averaged according to the histogram count. What results is a contour of average growth rate as a function of wavenumber and frequency which can then be compared directly to the spectral density functions from experiment.

Figure 6 shows the “growth” density functions created using the same data presented in Figure 5 separated into different bias groupings and parallel eigenvalue n . The growth density functions shown were averaged for three bias regions: Row (a)Bias 0-9 representing all the biases with flow in the IDD; (b)Bias 10-14 representing the region near zero flow and just into the EDD flow; and (c)Bias 15-29 representing moderate to strong EDD flow. The first column shows these growth density functions calculated for $n=0$ and the second for $n=0.5$. The negative signed wavenumbers indicate mode propagation in the IDD while positive signed wavenumbers indicate EDD. The features of these plots will be explored in more detail when being compared to experimental data.

To compare to the linear growth rate density functions shown in Figure 6, the spectral density plots for the same bias groupings and radial extent displayed in Figure 7.

A comparison of the two sets of plots yields similar overall features: 1) Both show an overall trend of mode propagation from the IDD to the EDD direction as bias is increased. In the experimental data there is a clear lean toward IDD wavenumbers in the low bias states. Similarly, in the growth density functions, the growth of modes is primarily in the IDD direction as well, form both

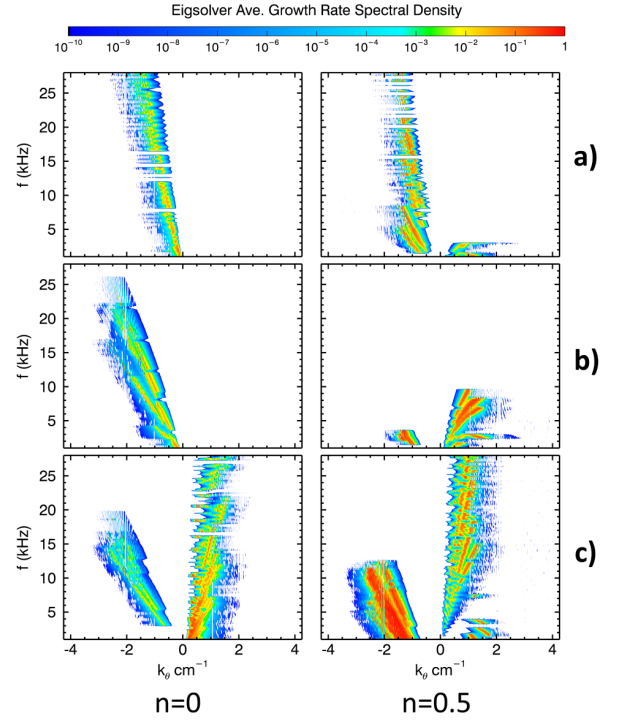


FIG. 6. Growth Density functions from linear eigensolver calculations for 3 bias groupings: (a)Bias 0-9, (b)Bias 10-14, and (c)Bias 15-29. Growth rates were restricted to the radial region of 20 to 32cm.

$n=0$ and $n=0.5$ parallel eigenvalues. The low bias spectral density plots due show some power in the EDD and the growth density plots show some growth at low frequency and wavenumber in the EDD direction as well—characteristic of drift wave modes. Additionally, both spectral density and growth density plots for the low bias states have values which increase in frequency space with increasing wavenumbers. 2)Both low/zero flow bias groupings show a shift in density magnitude from high frequency to low frequency values. The low flow spectral density plot shows very little power beyond 5-10kHz and appears to be more evenly distributed between IDD and EDD directions, though there is still a slight tilt in the IDD. Meanwhile, the growth density plots also show a shift to lower frequency especially in the $n=0.5$, IDD direction. Meanwhile, there is a concentration of growth density in the $n=0.5$, EDD direction. Since these middle biases correspond to the states of lowest flow, this growth is likely the emergence of a dominant drift-wave mode. 3)Moving into the high bias, high EDD flow regimes, there is a clear shift into EDD propagating modes. Direct comparison of the top and bottom plots of both spectral density and growth density highlight this change. The experimental data shows an overall lean to the EDD and the appearance of the coherent mode is clear between 8 and 12kHz where the red is darkest. Despite this overall shift, there is still significant fluctuations propagating in both directions; the width in wavenumbers space for frequencies less than 10kHz is generally wider than the low

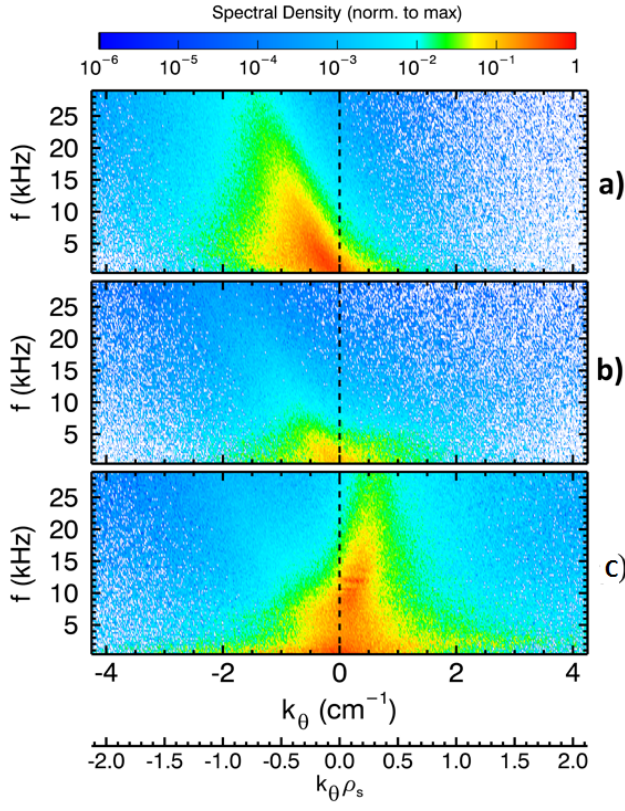


FIG. 7. Perp Wavenumber spectra for three different bias groupings in the 20-32cm region (a)Bias 0-9 (b)Bias 10-14, and (c)Bias 15-29.

bias groupings. In the calculated growth density plots, there is clearly more growth in the EDD for $n=0$, though growth in the IDD is not entirely eliminated. The $n=0.5$ column has the most activity with strong growth in both azimuthal directions. Since the high bias states have flow and density profiles that would both tend to drive their corresponding instability in the EDD, the strong growth in the IDD is a possible indication of KH growth.

To narrow down the possible origins of the features in both the spectral and growth density plots, cuts in radius and bias can be made to highlight the regions where only certain gradients are present. The first cut is made to radius in order to separate density gradient only regions from regions with density and flow. Figure 8 shows spectral density plots for all biases, but restricted to either 12-20cm (top) or 20-32cm (bottom); this cut-off in radius approximates where the rotation in the edge no longer penetrates into the core (even at the highest biases). The distinction is striking; turbulent fluctuations in the core region are broad in wavenumber space, spanning both azimuthal directions, but very restricted in frequency space, with fluctuation amplitude dropping by at least 3 orders of magnitude beyond 5kHz. The edge region, in contrast, is much more narrowly confined in wavenumber space, but expands into large frequencies, reaching significant amplitudes up to 20kHz.

Linear calculations appear to somewhat mirror this dif-

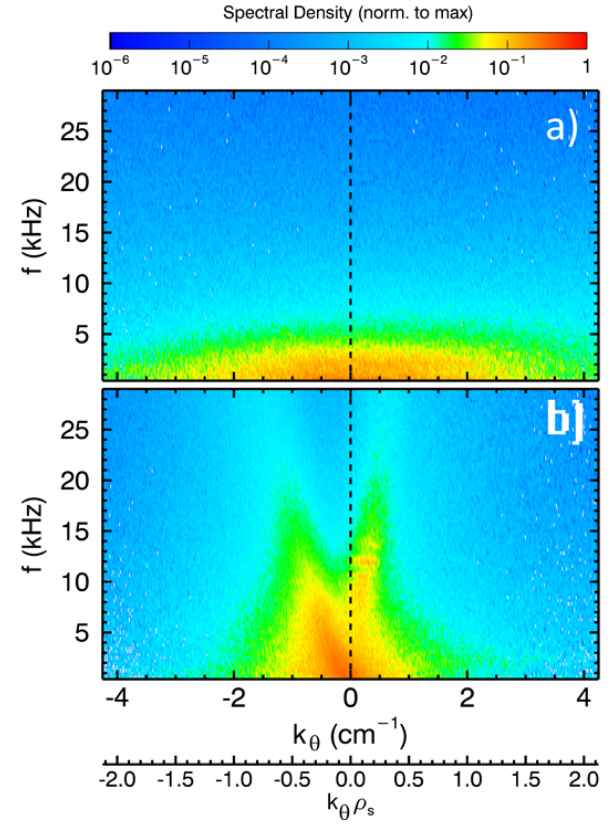


FIG. 8. Perp Wavenumber spectra for two different gradient regions (a)Density gradient only, no flow (12-20cm) and (b) Density gradient, temperature gradient, and flow (20-32cm).

ferences observed in the spectral density plots. Figure 9 shows the growth density for the same sets of biases in Figure 6, but restricted to modes that peak in the region 12 to 25cm, again where density gradients are the primary gradient drive. Comparison between these plots and those in Figure 6 show that without flow, the only modes that grow are those which were speculated to be drift-waves. Like the spectral density plots, the growth density plots are localized to low frequencies, less than 10kHz. The growth rate features in the IDD that spanned the large range in frequencies are not present, though there is some evidence of possible flow driven modes (this is possible since the cutoff for calculated growth is wider than the experimental cutoff and some flows exist in the 20 to 25cm region.) Assuming that $n=0.5$, EDD propagating modes in the top and middle row plots are indeed drift waves, the modes can be characterized by generally low frequency and for having a light curve in the apparent dispersion relation, as the frequency increase with wavenumber appears to level off. This then can be distinguished from the flow modes in Figure 6 which have a more linear dispersion relation. It should also be noted that while the bottom row of Figure 9 would seem to indicate no drift-wave growth despite the steepened gradient at high bias, the likely reason for this is that the density gradient is strongest in the region beyond 25cm for high biases; in fact, looking at the density profiles for

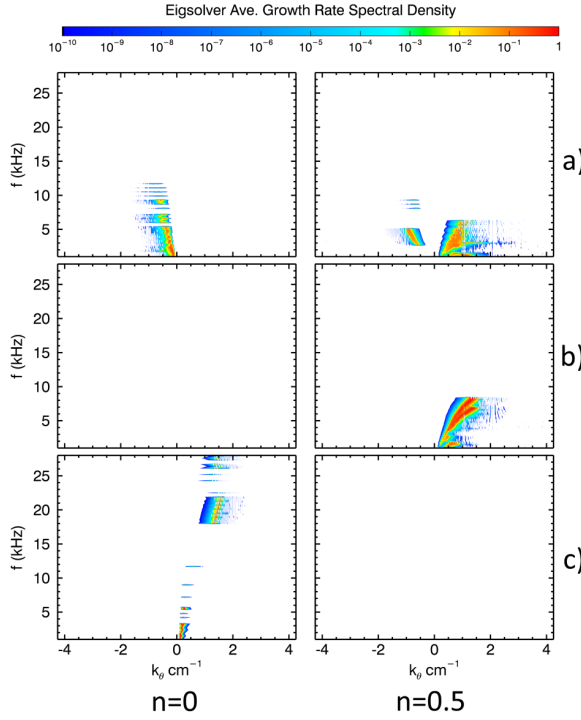


FIG. 9. Growth Density functions from linear eigensolver calculations for 3 bias groupings: (a) Bias 0-9, (b) Bias 10-14, and (c) Bias 15-29. Growth rates were restricted to the radial region of 12 to 25cm.

high bias show that there is comparatively little density gradient for high biases in the 12-20cm region. Looking instead at the edge growth density plots in Figure 6(c), there appears to be some drift-wave like mode growth in the region $< 5\text{ kHz}$, distinct from the flow driven modes in the higher frequency.

Since the main difference between these two regions is the presence or lack of a flow profile, while a density gradient is present throughout both, it is tempting to attribute the turbulent spectral density of Figure 8(a) as being generated by drift-wave turbulence; however, this is too simplistic a conclusion to make as other modes can be active, such as the non-linear modes mentioned earlier³². Trying to connect the nature of the turbulence in the core seen in the experiment to growing linear drift waves is impossible without taking into account these non-linear and saturation mechanisms. Indeed, the linear calculations show that linear drift waves should propagate in the EDD direction while the saturated turbulence is clearly symmetrically distributed. What can be concluded is that the introduction of flow has a significant impact on the eventual saturated turbulence either through the generation of pure rotational flute modes or through coupling to the modes already present (e.g. drift-interchange modes). The shape of the spectral density distribution in Figure 8(b) compares much more favorably to the growth rate distribution shape for the edge region modes in Figure 6 suggesting that these flow driven modes may retain more of their linear nature than the modes in the core. In

fact, it can will shown that the coherent modes observed in the driven states can be fairly conclusively attributed to the growth of both a pure ($n=0$) interchange mode and a coupled ($n=0.5$) drift-interchange mode.

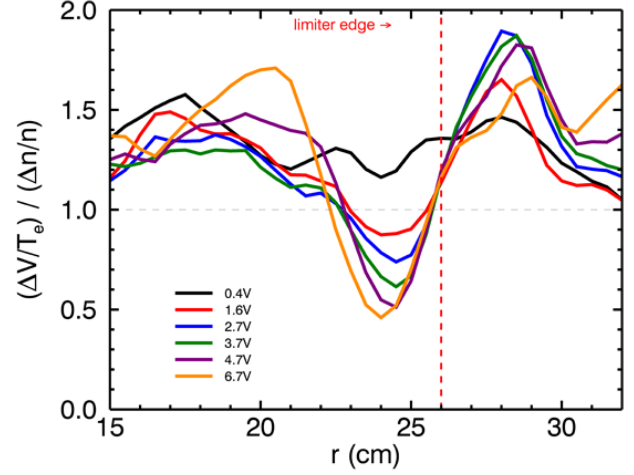


FIG. 10. Profiles of ratios of floating potential fluctuations to density fluctuations biases that exhibit a coherent mode as well as a strong vorticity gradient.

An attempt to distinguish between rotational interchange and Kelvin-Helmholtz modes can be made. Again referring to the edge spectral density plots in Figure 7, the modes that change direction from IDD to EDD are most likely to be driven by interchange. In the full range growth density plots, the IDD flow biases show significant growth in the IDD direction for both $n=0$ and $n=0.5$ which is indicative of interchange modes; however, it is conceivable that KH modes would be present as well. When the flow is reverse into the EDD, as in the bottom row plots, there is now significant EDD growth for both $n=0$ and $n=0.5$, consistent with rotational interchange modes driven by EDD flow; however there remains growth in the IDD. Since the flow is almost entirely in the EDD for these biases, the strong IDD growth probably cannot be RI, leaving KH as the likely candidate. This can be supported noting where KH drive is likely to exist. In Figure ??, the gradient of the vorticity reaches its largest values when the limiter is between 1 and 10V above the anode—corresponding to Biases 15-25—as well as localized in a region just outside the limiter edge. Similarly, the fluctuation ratio profiles shows peak values in this radial region for the bias range listed, shown in Figure 10. KH modes would generally have fluctuation ratios $R \gg 1$. While ratios just under 2 cannot be considered large, the higher values are consistent with KH drive in that region.

Finally, linear calculations also support the KH mode hypothesis. Figure 11 shows the growth density now restricted to the range 27.5 to 31cm and with biases grouped differently. The top plot is still low biases Bias 0-9, but the middle plot now averages Biases 15 to 25 and

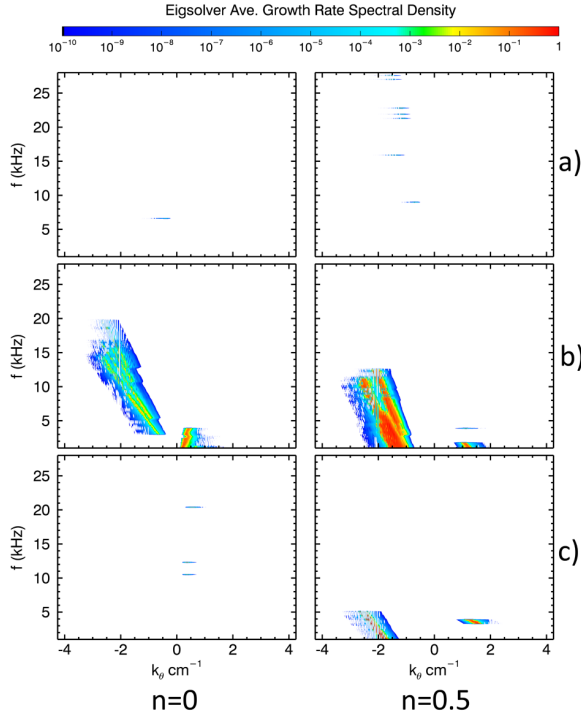


FIG. 11. Growth Density functions from linear eigensolver calculations for 3 bias groupings: (a)Bias 0-9, (b)Bias 15-25, and (c)Bias 27-29. Growth rates were restricted to the radial region of 27.5 to 31cm.

the bottom plot shows Bias 27 through 29. It is clear in comparison to the full range, bottom plot of Figure 6 that the modes growing in the IDD for both $n=0$ and $n=0.5$ really only grow in the biases and in the region that has significant vorticity gradient. This can be compared to spectral density plots for the same region and biases of Figure 12. Like the growth density plots, the spectral density does not exhibit the long linear features that presumably are characteristic of the rotational interchange modes. Rather they feature squatter shapes in frequency and wavenumber space similar to those growth density features in Figure 11.

Finally, given the categorization of the probable contributions for DW, RI, and KH modes, the origin of the coherent mode can be explored. Figure 2 shows the frequency spectra for various biases zoomed in to frequencies less than 50kHz and focused in the region right around the limiter edge, where the presence of the coherent mode is strongest. Compared to the minimum flow case (Limiter-Anode = -5.0V), where the fluctuation spectrum is broadband, a clear peaks in the spectra emerge starting at a Limiter-Anode voltage difference of 2.7V and increasing in power and frequency up to a voltage difference of 13.1V. The highest bias listed, with a voltage difference of 25.9V, shows a reduction in power and less distinct peaks.

The very localized nature of the coherent mode (or modes) can help in determining its underlying instability. The mode peaks at the limiter edge which is precisely

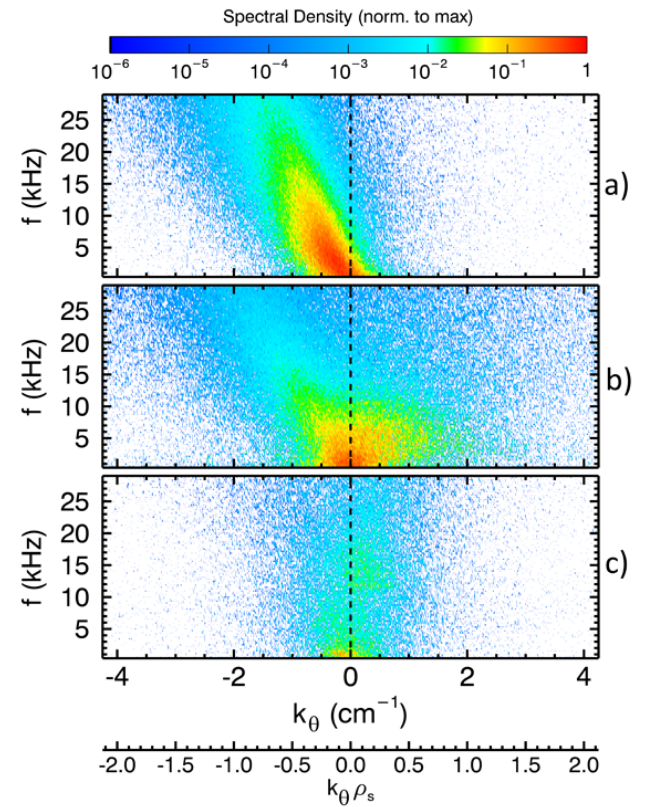


FIG. 12. Spectral density for (a)Bias 0-9, (b)Bias 15-25 and (c)Bias 27-29 restricted in the region outside the limiter edge, 27.5 to 31cm.

where the azimuthal flow peaks (see Figure ??) suggesting this mode is purely rotation interchange driven; however, the density profiles show that this point is also where the steepest density gradient occurs implying the strongest drive for drift waves would also occur at this point.

Given the lack of strong flow shear at this point ($\gamma_s = 0$ at the flow max), the mode is unlikely driven by the Kelvin-Helmholtz instability. It was also shown in Figure 11 that the KH drive appears to be localized to a region outside the limiter edge.

Since the coherent mode is generally observed in the same biases where the vorticity gradient peak is observed, Figure 10, shows that the fluctuation ratio for the limiter edge region sit fairly consistently at a value just above 1, consistent with what would be expected for interchange modes.

Spectrally, the mode does not begin to emerge as a distinctly coherent mode until the plasma is rotating in the EDD direction. Indeed, as shown in Figure 13(c) which shows the average spectral density for all the EDD flow states, the peaks in the spectra density indicating the coherent mode are situated only in the EDD propagation direction. Neither (a) or (b), representing the IDD flow or non-rotating bias states show coherent mode behavior. However, this directionality cannot rule out contribution from drift waves to the mode.

Comparison with the linear calculations, however, ap-

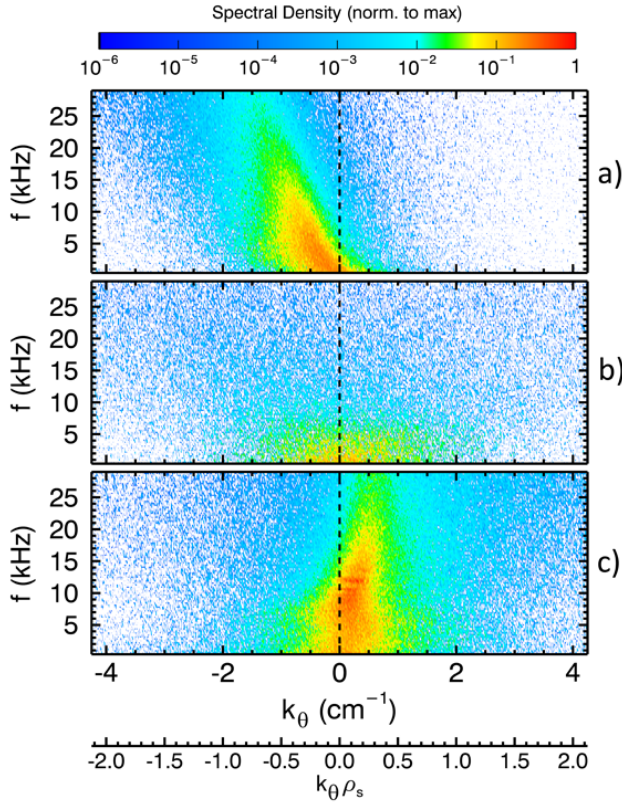


FIG. 13. Spectral density for (a)Bias 0-9, (b)Bias 10-14 and (c)Bias 15-29 restricted in the region right around the limiter edge, 24 to 28cm.

pears to offer the clinching evidence for rotational interchange. Figure 14 shows a similar set of growth density plots and bias groupings as in Figure 6, but restricted now to 24 to 28cm. Again for the regions of flow, the top and bottom plots, the only growth rate shown are those characteristic of rotational interchange modes. The $n=0.5$, high bias bottom right plot does not show features characteristic of the IDD KH modes or the low frequency EDD DW modes. The only growth in this region is due to rotational interchange modes; however, there is growth for both $n=0$ and $n=0.5$ modes. Which of these modes then drives the coherent mode?

The frequency of the calculated modes can be examined and compared to the experimental frequency peaks from the measured spectra. Returning to the original forms of the calculated values of growth rate and frequency as in Figure 5, the frequency of the fastest growing m number mode for each frequency and for both $n=0$ and $n=0.5$ is plotted against limiter bias in Figure 15. Close examination of the frequency spectra shows that there are actually two peaks that begin to appear with EDD flow; one at a lower frequency and one at a higher one. For example, the blue curve in Figure 2 exhibits a clear peak at a frequency of about 7kHz as indicated by the dotted line, but a second peak at about 2kHz can also be seen. With increasing bias, the frequencies of both peaks increase, with the one starting at a lower

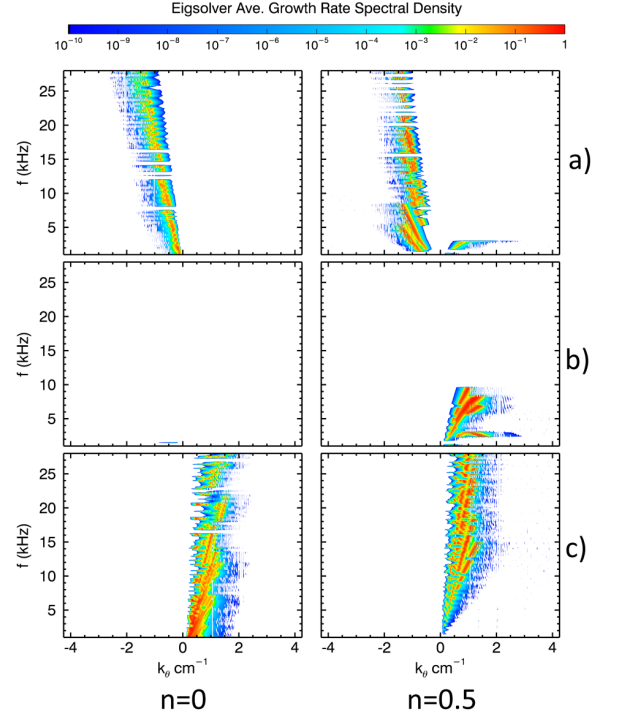


FIG. 14. “Growth” Density functions from linear eigensolver calculations for 3 bias groupings: (a)Bias 0-9, (b)Bias 10-14, and (c)Bias 15-29. Growth rates were restricted to the radial region of 24 to 28cm which surrounds the limiter edge and location of the coherent mode.

frequency originally increase slightly faster than the high frequency peak. As the frequencies merge, there appears to be a mode interaction and sidebands appear resulting in multiple peaks. The red and green curves of Figure 2 show this behavior. The multiple peaks are plotted as a function of limiter bias in 15 indicated by the small red dots. For low bias voltages, the peak is just taken as the peak of the broadband spectra. As more distinct peaks emerge, there appears to be two lines of increasing frequency forming with increasing bias. At a limiter minus anode voltage of about 5V, more than two peaks begin to appear and the two lines merge into a range of peaks which continue to increase in frequency with bias.

The experimental peaks can be then compared to the frequencies of the fastest growing modes for each bias. Since the linear growth rates do not incorporate any saturation mechanisms, a limit on the range of m numbers must be set manually. Referring to the experimental m eigenvalue distributions in Figure 4, it is clear that the fluctuations power as a function of m number falls off by about an order of magnitude by about $m=25$. The top plot in 15 shows the frequency for the fastest growing m number mode within this $m=1-25$ range. The frequency of the fastest growing $n=0$ modes appear to generally follow the lower frequency line of experimental peaks. The fastest growing $n=0.5$ growing modes though tend to outpace the increase in frequency of the second experimental line. However, by limiting the m number range

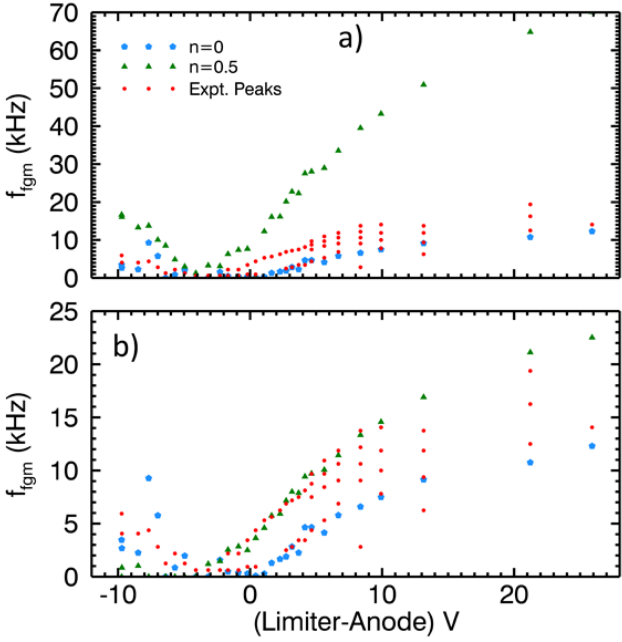


FIG. 15. Linear eigensolver calculated fastest growing modes for each bias state for $n=0$ (blue pentagon) and $n=0.5$ (green triangle) with peaks in the experimental spectra of each bias (red circles). If the spectra show multiple distinct peaks, a red circle is placed to indicates the frequency of each peak. The top plot (a) shows frequency of the maximum growing m -number mode per bias with m -number restricted to 1-25 for both $n=0$ and $m=1-25$ for $n=0.5$. The bottom plot (b) is the same, but with the range restricted to $m=1-25$ for $n=0$ and $m=1-7$ for $n=0.5$. These restrictions are motivated by the experimental m -numbers measured.

of the calculated fastest growing mode, the frequency of the $n=0.5$ modes can be reduced. The bottom plot displays the same data as the top, but with m numbers for the $n=0.5$ modes restricted to $m=1-7$. Forcing this low m number is not entirely unreasonable considering that the experimental m -number peak for limiter edge fluctuations as seen in Figure 4(b) is just under $m=10$. Given this restriction the $n=0.5$ calculated frequencies line up almost exactly with the line of high frequency experimental peaks.

Figure 16 shows calculated eigenfunctions for given m and n eigenvalues compared to a frequency filtered density profile which can serve as an experimental radial eigenfunction. Figures 16(a) and (c) show the radial eigenfunctions for two lower frequency, $n=0$ modes while (b) and (d) show the eigenfunctions for two higher frequency $n=0.5$ modes. The m -numbers of the modes correspond to the fastest growing mode m -number as indicated by Figure 15(b). The experimental density fluctuation profile is filtered to a small bandwidth that nearly matches the frequency of the fastest growing mode. The comparison shows that for (b) and (d) that the peak of the eigenfunction corresponds to the peak of the experimental fluctuation profile. On the other hand, plots (a) and (c) show that the eigenfunction match up to a local

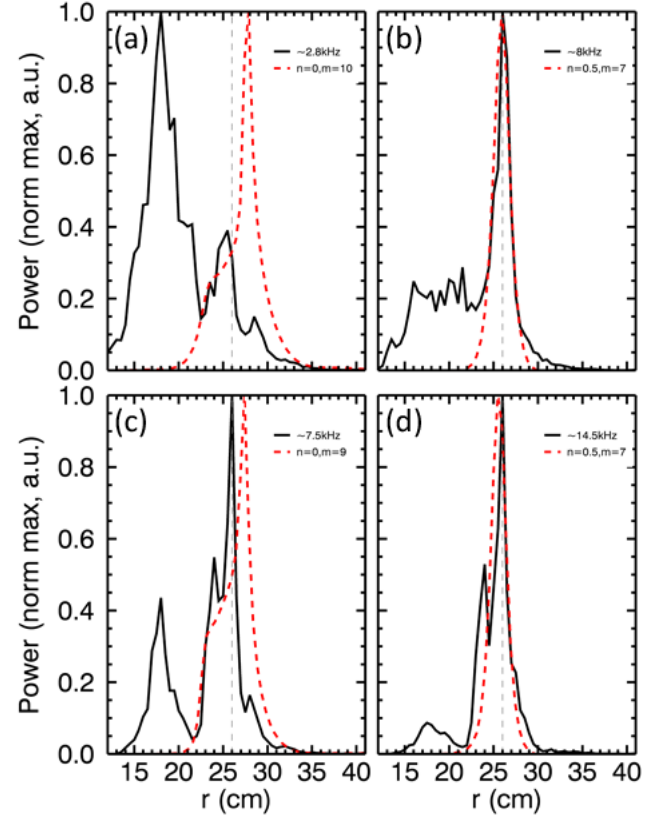


FIG. 16. Comparison of radial eigenfunctions calculated using the Braginskii eigenmode solver with filtered density fluctuation profiles. (a) Shows the eigenfunction (red) for the fastest growing mode for $n=0$ for a moderately biased, medium EDD flow case, which is also found to have $m=10$ and a frequency of about 2kHz. The density fluctuation profile (black) for his same bias is bandwidth filtered just around 2kHz. (b) Shows a similar plot for this same bias case but for the fastest growing $n=0.5$ mode which has an $m=7$ and frequency of 8kHz. (c) and (d) show the same as (a) and (b) but for a high bias, high EDD flow case.

peak, but not peak with the most power. This suggests that the $n=0$ modes—(a) and (c)—correspond to a peak just outside the limiter edge while the $n=0.5$ modes—(b) and (d)—correspond to a peak directly on the limiter edge.

The conclusion from this analysis is that the coherent mode observed at the limiter edge is in fact two coherent modes; one driven by pure $n=0$ rotational interchange and the other driven by $n=0.5$ rotational interchange. Since the parallel eigenvalue of this second mode is non-zero, it is in a way coupling to the mechanism that drives drift-waves. Thus non-zero parallel eigenvalue rotational modes are often called drift-interchange modes. As the rotation, and thus drive and frequency of these modes, increases, the interchange and drift-interchange modes appear to interact creating multiple sideband peaks. At even high biases, this linear interaction seems to evolve into non-linear broadband turbulence. In the highest measured bias spectra, shown as the purple line in Fig-

ure 2, the intensity of the coherent mode has collapsed, turning into a more broadband like structure, and its energy possibly going into high frequency values. Comparison of the radial location of peaks between Figures 16(a) and (c) also seems to show that the radial location of the $n=0$ mode begins to shift slightly inward with increasing bias. This is likely a contributing cause to the increasing interaction and sideband production.

The results of this mode analysis suggest that the saturated LAPD plasma consists of a combination of low frequency drift modes overlayed with higher frequency linear rotational interchange and drift wave modes. All plasma states appear to share a common bed of low frequency ($<5\text{kHz}$), broadband fluctuations approximately equally distributed in both electron and ion diamagnetic drift directions, most likely saturated drift-wave turbulence. If rotation is present in any amount, higher frequency (5-15kHz) modes appear on top of this broadband foundation. In the unbiased state, these rotational interchange modes propagate in the ion diamagnetic drift direction and remain broadband in nature as reflected in both frequency spectra and spectral density. In strongly biased states, while the low frequency drift-wave base remains, a higher frequency coherent mode emerges out of the broadband spectrum as well as the appearance of KH modes. The coherent modes are a rotational interchange and rotational drift-interchange mode that can be seen to grow up, interact and eventually spread out into additional broadband turbulence.

V. CONCLUSIONS

The authors would like to thank Zoltan Lucky and Marvin Drandell for their valuable technical support. This work was supported by the National Science Foundation (PHY-0903913) and performed using the Basic Plasma Science Facility at UCLA. The BaPSF is funded by the Department of Energy and NSF.

¹K. Burrell, Phys. Plasmas **4**, 1499 (1997).

²K. Burrell, Phys. Plasmas **6**, 4418 (1999).

³P. Terry, Rev. Mod. Phys. **72**, 109 (2000).

⁴G. Van Oost , J. Adamek and V. Antoni, P. Balan, J.A. Boedo, P. Devynck, I. Duran, L. Eliseev, J.P. Gunn, M. Hron, C. Ionita, S. Jachmich, G.S. Kirnev, E. Martines, A. Melnikov, R. Schrittwieser, C. Silva, J. Stockel, M. Tendler, C. Varandas, M. Van Schoor, V. Vershkov and R.R. Weynants, Plas. Phys. Control Fusion **48**, 621 (2003).

⁵O. Sakai, Y. Yasaka and R. Itatani, Phys. Rev. Lett. **70**, 4071 (1993).

- ⁶J.E. Maggs, T.A. Carter and R.J. Taylor, Phys. Plasmas **14**, 052507 (2007).
- ⁷T.A. Carter and J.E. Maggs, Phys. Plasmas **16**, 012304 (2009).
- ⁸D.A. Schaffner, T.A. Carter, G.D. Rossi, D.S. Guice, J.E. Maggs, S. Vincena and B. Friedman, Phys. Rev. Lett. **109**, 135002 (2012).
- ⁹K.H. Burrell, T.N. Carlstrom, E.J. Doyle, D. Finkenthal, P. Goihil, R.J. Groebner, D.L. Hillis, J. Kim, H. Matsumoto, R.A. Moyer, T.H. Osborne, C.L. Rettig, W.A. Peebles, T.L. Rhodes, H. St.John, R.D. Stambaugh, M.R. Wade and J.G. Watkins, Plas. Phys. Control Fusion **34**, 1859 (1992).
- ¹⁰F. Wagner, Plas. Phys. Control Fusion **49**, B1 (2007).
- ¹¹R.J. Taylor, M.L. Brown, B.D. Fried, H. Grote, J.R. Liberati, G.J. Morales, P. Pribyl, D. Darrow and M. Ono, Phys. Rev. Lett. **63**, 2365 (1989).
- ¹²R.R. Weynants, G. Van Oost, G. Bertschinger, J. Boedo, P. Brys, T. Deligne, K.H. Dippel, F. Durodie, H. Euringer, K.H. Finken, D.S. Gray, J.D. Hey, D.L. Hillis, J.T. Hogan, L. Konan, R. Leners, A.M. Messian, A. Pospieszczyk, U. Samm, R.P. Schorn, B. Schweer, G. Telesca, R. Vannieuwenhove and P.E. Vandenplas, Nucl. Fusion **32**, 837 (1992).
- ¹³R.R. Weynants, S. Jachmich and G. Van Oost, Plas. Phys. Control Fusion **40**, 635 (1998).
- ¹⁴J. Boedo, D. Gray, S. Jachmich, R. Conn, G.P. Terry, G. Tynan, G. Van Oost, R.R. Weynants and TEXTOR Team, Nucl. Fusion **40**, 7 (2000).
- ¹⁵J.A. Boedo, D.S. Gray, P.W. Terry, S. Jachmich, G.R. Tynan, R.W. Conn and TEXTOR-94 Team, Nucl. Fusion, **42**, 117 (2002).
- ¹⁶H. Biglari, P.H. Diamond and P.W. Terry, Phys. Fluids B. **2**, 1 (1990).
- ¹⁷K.C. Shaing, E.C. Crume and W.A. Houlberg, Phys. Fluids B **2**, 6 (1990).
- ¹⁸Y.Z. Zhang and S.M. Mahajan, Phys. Fluids B **4**, 1385 (1992).
- ¹⁹Y.Z. Zhang and S.M. Mahajan, Phys. Fluids B **5**, 7 (1993).
- ²⁰A.S. Ware, P.W. Terry, P.H. Diamond and B.A. Carreras, Plasma Phys. Control Fusion **38**, 1343 (1996).
- ²¹A.S. Ware, P.W. Terry, B.A. Carreras and P.H. Diamond, Phys. Plasmas **5**, 173 (1998).
- ²²P.W. Terry, D.E. Newman and A.S. Ware, Phys. Rev. Lett. **87**, 185001 (2001).
- ²³E.-J. Kim and P.H. Diamond, Phys. Rev. Lett. **90**, 7 (2003).
- ²⁴E.-J. Kim, P.H. Diamond and T.S. Hahm, Phys. Plasmas **11**, 10 (2004).
- ²⁵A.P.L. Newton and E.-J. Kim, Phys. Plasmas **18**, 052305 (2011).
- ²⁶W. Gekelman, H. Pfister, Z. Lucky, J. Bamber, D. Leneman and J. Maggs, Rev. Sci. Instrum. **62**, 2875 (1991).
- ²⁷T.S. Hahm, Phys. Plasmas **1**, 2940 (1994).
- ²⁸M. Leconte, P. Beyer, S. Benkadda and X. Garbet, Phys. Plasmas **13** 112301 (2006).
- ²⁹A.P.L. Newton and E.-J. Kim, Phys. Plasmas **14**, 122306 (2007).
- ³⁰P.W. Terry and R. Gatto, Phys. Plasmas **13**, 062309 (2006).
- ³¹G.M. Staebler, R.E. Waltz, J. Candy and J.E. Kinsey, Phys. Rev. Lett. **110**, 055003, (2013)).
- ³²B. Friedman, T.A. Carter, M.V. Umansky, D. Schaffner and B. Dudson, Phys. Plasmas **19**, 102307 (2012).
- ³³M. Umansky *et al.*, Phys. Plasmas **18**, 055709 (2011).
- ³⁴P.Popovich, M.V. Umansky, T.A. Carter and B. Friedman, Phys. Plasmas **17**, 122312 (2010).